Composites Part B 279 (2024) 111445

Contents lists available at ScienceDirect

Composites Part B

journal homepage: www.elsevier.com/locate/composites

Effect of temperature on high strain-rate damage evolving in CFRP studied by synchrotron-based MHz X-ray phase contrast imaging

Xiyao Sun [a], David Sory [a], Kai Liu [a], Bratislav Lukić [b,c], David Simonian [a], Kwan Lok Wong [a], Alexander Rack [b], David Chapman [a], Nik Petrinic [a], Daniel Eakins [a,*]

[a] Department of Engineering Science, University of Oxford, Parks Road, Oxford, OX1 3PJ, UK
[b] European Synchrotron Radiation Facility, 71 Av. des Martyrs, Grenoble, 38000, France
[c] Henry Royce Institute for Advanced Materials, Department of Materials, The University of Manchester, Manchester, M13 9PL, UK

ARTICLE INFO

Keywords:
A. Polymer-matrix composites (PMCs)
B. Impact behaviour
B. Low-temperature properties
C. Damage mechanics
Synchrotron X-ray phase-contrast

ABSTRACT

The present study demonstrates experimental evidence of subsurface mesoscale damage initiation and evolution in angle-ply CFRP laminates under high strain-rate loading at low temperatures using synchrotron-based X-ray MHz radiography. A bespoke set of loading, temperature control and *in-situ* X-ray imaging systems were applied to simultaneously correlate high strain-rate mechanical response with observed subsurface damage in a time-resolved manner. The results demonstrate that independent of temperature, damage evolved following a specific sequence; firstly intra-ply shear cracking along the fibre direction, developing into multi-layer cracking with continued deformation, and finally culminating in inter-ply delamination and complete failure of the specimen. The timescale for this sequence, however, was observed to strongly depend upon temperature, with low temperatures resulting in more rapid damage evolution and loss of mechanical strength.

1. Introduction

To respond to global environmental policies, a wide range of modern transport industries, such as aerospace, automobile and maritime, have invested heavily in the research and application of carbon-fibre reinforced polymer (CFRP) composites due to their high stiffness and strength-to-weight ratio over conventional metal-based alternatives [1–3]. In such applications, CFRP components can be exposed to a multitude of adverse conditions, including extremes of mechanical loading, humidity and temperature. However, understanding of the behaviour of CFRP under such complex and often combined conditions is incomplete, which is hindering CFRP composites from being more widely used in future industrial products.

There are ample studies exploring the strain-rate sensitivity of epoxy-based CFRP laminates at room temperature [4–7]. For extreme temperatures, it has been found that the tensile [8–13] and bending [14] performance of CFRP is susceptible to temperature change. In addition, thermal cycling can also lead to strength degradation for CFRP laminates because of the generated micro-damage between fibre and matrix as the result of their differing thermal expansion characteristics [15].

The failure of CFRP could be sudden and catastrophic due to its well-known brittleness [16–19]. [0/90] cross-ply (CP) [4], [±45] angle-ply (AP) [20], quasi-isotropic (QI) [5] and 90° off-axis biaxial braided (BB) [21] CFRP laminates have been observed to fail by inter-ply delamination under in-plane compression with different strain-rates (confirmed via post-mortem examination using visual and computed tomography (CT), and *in-situ* examination using visible light and infrared thermal imaging). Previous investigation of CFRP laminates tested at *in-situ* extreme temperature indicates both high and low temperatures can weaken the fibre/matrix bonding at the interface. Where, for example under tensile loading at quasi-static (QS) and intermediate strain-rates, more pronounced fibre debonding and laminate delamination was observed in postmortem inspection relative to room temperature testing [8,13]. Under flexural loading (three-point bending), damage in CFRP specimens has been shown to propagate faster and expand wider at lower temperatures, causing more severe delamination [14].

X-ray imaging, especially X-ray CT, has become an important technique to non-destructively investigate the internal structures of composite components and damage [22,23]. Instead of only performing post-mortem scanning, recent developments have enabled *in-situ* CT scanning to characterise internal structural changes under loading induced

* Corresponding author.
E-mail addresses: xiyao.sun@eng.ox.ac.uk (X. Sun), daniel.eakins@eng.ox.ac.uk (D. Eakins).
URL: https://shock.eng.ox.ac.uk (D. Eakins).

https://doi.org/10.1016/j.compositesb.2024.111445
Received 22 January 2024; Received in revised form 5 March 2024; Accepted 9 April 2024
Available online 20 April 2024

Table 1
Specimen pretreatment and testing conditions.

Specimen label	Pretreatment condition	Appx. impact velocity, m/s	Testing temperature, °C
Dry_Room	Oven dried	11.0	23 ± 2
Dry_Low	Oven dried	11.0	-30 ± 2
Cycled_Room	250-time HTC cycled	15.5	23 ± 2
Cycled_Low	250-time HTC cycled	15.5	-30 ± 2

* HTC: hygrothermally cycled.

by tension [24], compression [25], flexure [26] and wedge indentation [27]. Apart from that, some recent research has also demonstrated that synchrotron-based dynamic X-ray imaging has a great potential to probe the subsurface damage of composites under high strain-rate (HSR) loading [28,29].

While a limited number of studies have visualised the initiation and evolution of damage in CFRP laminate under HSR loading [28,29], no studies have resolved the *in-situ* progression of mesoscale subsurface damage at low temperatures. Direct experimental evidence would greatly enhance both existing and future simulation models used to predict the HSR failure of CFRP laminates. In this study, a synchrotron-based X-ray source, together with a bespoke set of synchronised loading, temperature control, strain measurement, ultra-fast X-ray imaging and data acquisition system, was implemented to achieve real-time mesoscale damage probing and property measurement for tested specimens at HSR loading. Synchrotron-based X-ray phase-contrast imaging (XPCI) was introduced as it facilitates the visualisation of damage and fine features (*e.g.*, newly generated interface) due to phase contrast enhancement. A group of AP CFRP specimens with different ageing conditions were prepared and tested under HSR in-plane compression at room and low temperatures. The subsurface damage development and associated mechanical behaviours were characterised and analysed integratively in a time-resolved manner. Finally, the failure micromechanics and models of tested CFRP laminates were deduced and discussed.

2. Materials and methods

2.1. Material and specimen

The material studied in this work is an aerospace-grade epoxy-based carbon-fibre reinforced polymer composite (CFRP) that is comprised of autoclave-cured laminates with a curing cycle of 1–2 °C/min heating rate, 2–5 °C/min cooling rate, and 120-min duration at 180 °C. It was manufactured by using the hand lay-up method with $[\pm 45]_{4s}$ AP laminations and cut into a size of $5 \times 5 \times 3$ mm^3 for effective environmental ageing and HSR loading. Two ageing conditions were considered in the present research — dry and hygrothermally cycled (see Table 1). The dried specimens were oven-dried following ASTM standard 5229 [30] at 70 °C for four weeks until no further weight could be reduced. The cycled CFRP specimens were saturated in an environmental chamber following the same ASTM standard at 70 °C with a constant relative humidity of 85% for four weeks to ensure complete saturation before cycling. After full saturation, the CFRP specimens were subjected to 250 sequential temperature cycles between −50 and 90 °C. Each cycle took about 150 min, with the 250 cycles therefore taking approximately 1 month to complete. Specimens with a higher number of cycles were also prepared, tested and analysed. However, their differences in terms of mechanical properties and damage mechanisms were found to be trivial compared to 250-time cycled specimens. Thus, only the results of 250-time cycled specimens are presented and discussed as a representation of cycled specimens in this work. Following controlled ageing, the internal configuration for each component (fibres, matrix and voids) and possible defects caused by manufacture and ageing were inspected by synchrotron-based X-ray μCT (2.1 μm) at beamline ID19 at the ESRF.

2.2. High strain-rate loading

HSR loading was applied using a split-Hopkinson pressure bar (SHPB) system [31]. As shown in Figs. 1 and 2, this SHPB setup consisted of a striker, input and output bars made of titanium alloy (Ti-6Al-4V) with a diameter of 12.7 mm. Ti-6Al-4V was adopted considering the high strength and mechanical impedance of the CFRP specimen studied in this work. The striker was 150 mm in length, and the input and output bars were 1300 mm and 1100 mm long, respectively. Before loading, two 3 mm-thick loading platens made of the same material and diameter as the bars were attached at the bar ends and in contact with the specimens to avoid damage to the bars. The specimens were sandwiched between the input and output bars with a thin layer of grease applied at the specimen/platen and bar/platen interfaces to reduce friction. A set of strain gauges was mounted 60 mm uprange of the specimens on the input bar and 40 mm downrange of the specimens on the output bar to record the incident, reflected, and transmitted strain pulses.

2.3. Test temperature control

A bespoke cryogenic chamber was designed and manufactured to enable good temperature isolation and impact debris containment whilst ensuring minimal X-ray beam attenuation. The chamber was constructed of Perspex and consisted of an inner and outer chamber. During the tests the temperature within the inner chamber was controlled by injecting cooled nitrogen gas using a Cobra Nitrogen Cooler from Oxford Cryosystems. The outer chamber was filled with room-temperature helium gas to prevent frost from forming on the X-ray window and introducing phase artefacts at the detector plane perturbing the X-ray image (Figs. 1 and 2). The temperature in the inner and outer chambers was measured and recorded from multiple measurement points and monitored from both the experimental hutch and control room.

2.4. High-speed X-ray imaging

Real-time visualisation of the evolution of impact initiated damage was performed at the ID19 beamline of the ESRF [32]. The SHPB system was aligned perpendicular to the X-ray beam path, as illustrated in Figs. 1 and 2, allowing the X-ray pulse train to propagate through the specimens normal to the direction of loading. In the present study, the 4 bunch fill mode was used, and the X-ray source at ID19 was a pair of aligned U32 undulators, producing a train of polychromatic X-ray pulses separated in time by 704 ns (“white-beam” with peak in the X-ray spectrum at about 23 keV). The indirect single-bunch X-ray imaging strategy employed in the current study is discussed in greater detail by Escauriza et al. [33]. Briefly however, the imaging system employed a 500 μm thick LYSO:Ce (Ce-dopped $Lu_{1-x}Y_xSiO_5$, Hilger Crystals, UK) single-crystal scintillator with 40 ns decay time, optically relayed to a pair of Shimadzu HPV-X2 high-speed cameras as illustrated in Figs. 1 and 2. Each optical relay consisted of a pair of Nikon 50 mm F/1.4 lenses producing an effective 1 × magnification with 0.34 numerical aperture. This indirect X-ray detector assembly was placed ~9 m downstream of the specimen to allow sufficient propagation distance for phase-contrast to form and hence enhance the

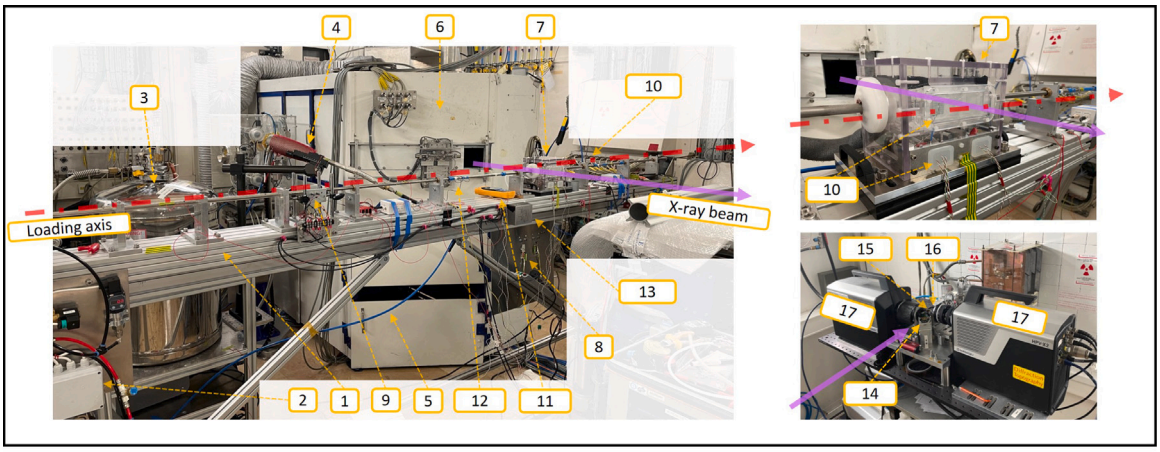

1. SHBP
2. Gas gun control valve
3. Liquid Nitrogen Dewar
4. Liquid Nitrogen injector
5. Helium gas injector
6. Syntrochron X-ray source
7. Double layer impact and temperature control chamber
8. Bespoke temperature control panel
9. Laser light gates
10. Temperature measurement
11. Temperature reader
12. Strain gauges
13. Gauge bridge box
14. Pellicle beamsplitter
15. LYSO:Ce Scintillator
16. Mirror
17. High-speed cameras

Fig. 1. Photos of the experimental setup, comprising the SHPB system, cryogenic impact chamber, and imaging system, at ID19, ESRF.

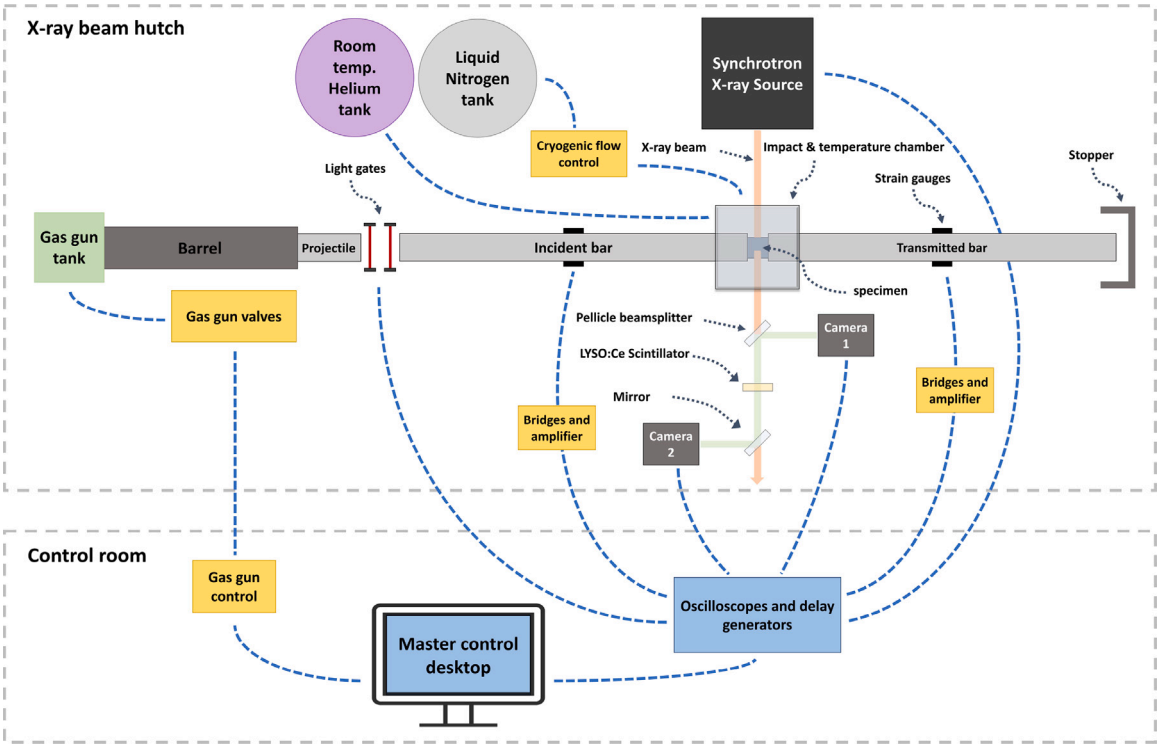

Fig. 2. Schematic of the experimental setup at ID19, ESRF, illustrating the key devices, components, connections, and beam paths of the SHPB and diagnostic systems.

visualisation of crack interfaces. The Shimadzu cameras were synchronised to the X-ray pulse train using the methods described in [33]. The 600 ns exposure of each camera captured scintillator emission primarily from a single X-ray bunch, and the camera triggering and frame rate (interframe time 1410 ns) were implemented such that the image sequences from the two cameras were interleaved in time to capture every bunch. The Shimadzu cameras were triggered from the voltage signals produced by the strain gauges on the input bar of the SHPB, enabling synchronisation of the radiography to the load history of the specimen. Finally, a fast X-ray shutter, gated open during the dynamic event, was used to reduce the total X-ray exposure duration to approximately 200 ms to minimise radiation-induced degradation of the specimen.

2.5. Mechanical property analysis

The stress–strain response of the specimens during HSR loading was estimated by assuming one-dimensional wave propagation [31]. The force recorded in the input and output bars was compared to evaluate force equilibrium. The engineering strain of the tested specimens obtained by processing the strain gauge signals was checked against the image measurements of the captured XPCI radiography. The bar energy

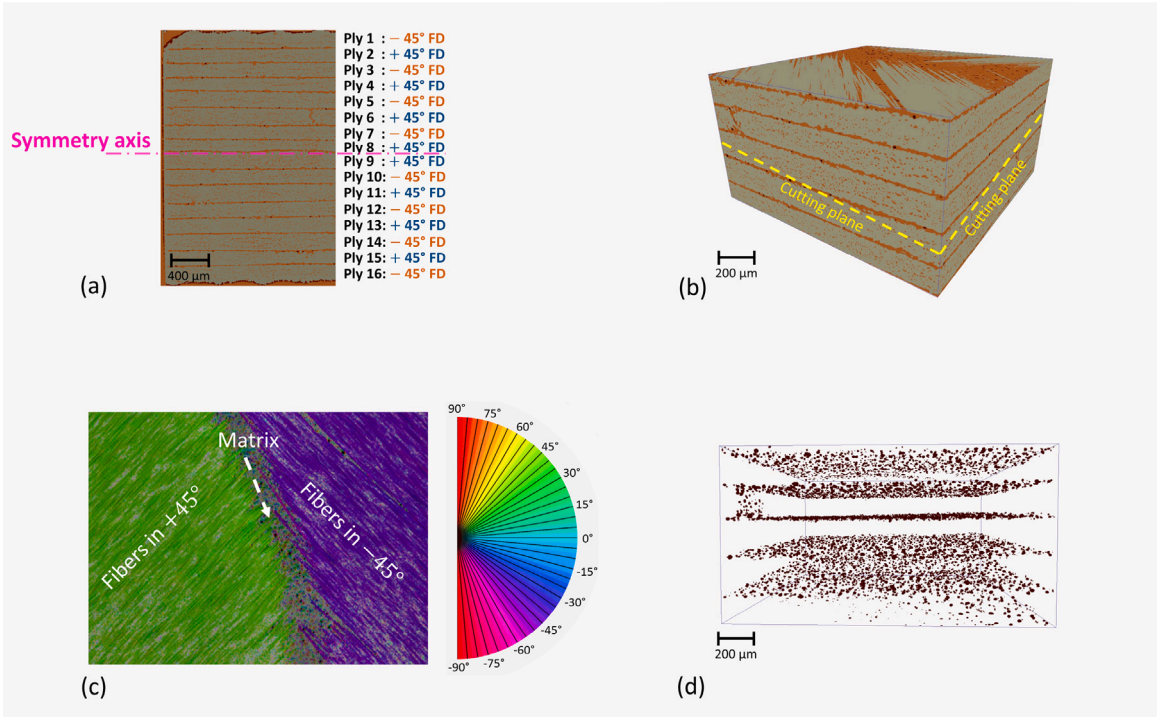

Fig. 3. Internal structural characterisation and defect checking for XPCI by using X-ray CT scanning: (a) an orthogonal slice with ply lay-ups, (b) volume rendering of a small specimen section with image segmentation, (c) fibre orientation identification on the cutting plane with the colour code performed by using OrientationJ plugin in ImageJ, and (d) segmented voids that distribute in the glue layers between plies. (For interpretation of the references to colour in this figure legend, the reader is referred to the web version of this article.).

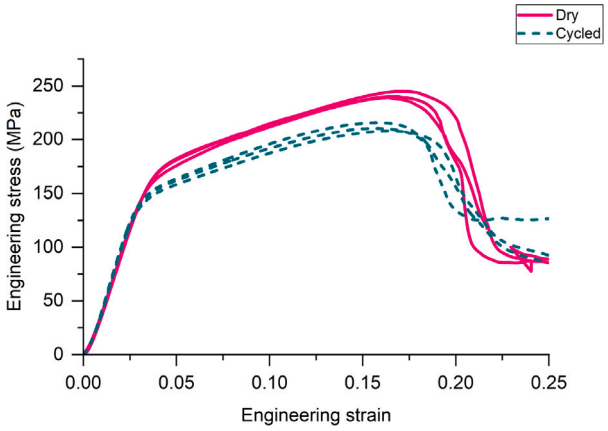

Fig. 4. Stress–strain curve of dried and cycled specimens under quasi-static (3.3×10^{-3} s^{-1}) uni-axial compression at room temperature setting a baseline for high strain-rate property analysis.

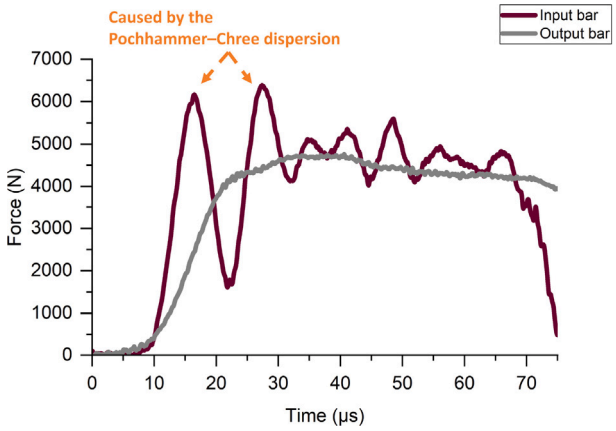

Fig. 5. Force equilibrium demonstrated by comparing force recorded in the input (incident and reflected wave) and output (transmitted wave) bar. Pochhammer–Chree dispersion was recorded in the input bar because no pulse shaper was used.

dissipated through the specimens, W, was also analysed by integrating the load–displacement curve, *i.e.*,

$$W = \int_0^{\delta_i} F_i(\delta_i)\, d\delta_i, \tag{1}$$

where F_i is the load acting on the material associated with the displacement δ_i.

2.6. Resolved damage analysis

Synchrotron-based dynamic XPCI is susceptible to fixed-pattern noise which can arise from aging and damage of optical elements (windows, lenses, scintillators), non-uniformities in the sensors (*i.e.*, the cameras in the present study) and in-homogeneities in the X-ray beam [34]. In order to aid crack identification, the obtained X-ray radiographs were subjected to a flat-field correction following,

$$I_c(t) = \frac{I_r(t) - \overline{I}_d}{\overline{I}_f - \overline{I}_d}, \tag{2}$$

where I_c stands for the 2D intensity of the flat-field corrected image at impact time t. I_r is the image intensity of the recorded image. Average flatfield $\overline{I}_f$ and darkfield $\overline{I}_d$ images were constructed from images taken with X-ray illumination but without objects, and images without both X-ray illumination and objects respectively.

Identification of the observed cracks at their initiation stage was performed by using a modified 2D image intensity analysis [27], while further details of their propagation and damage evolution was achieved

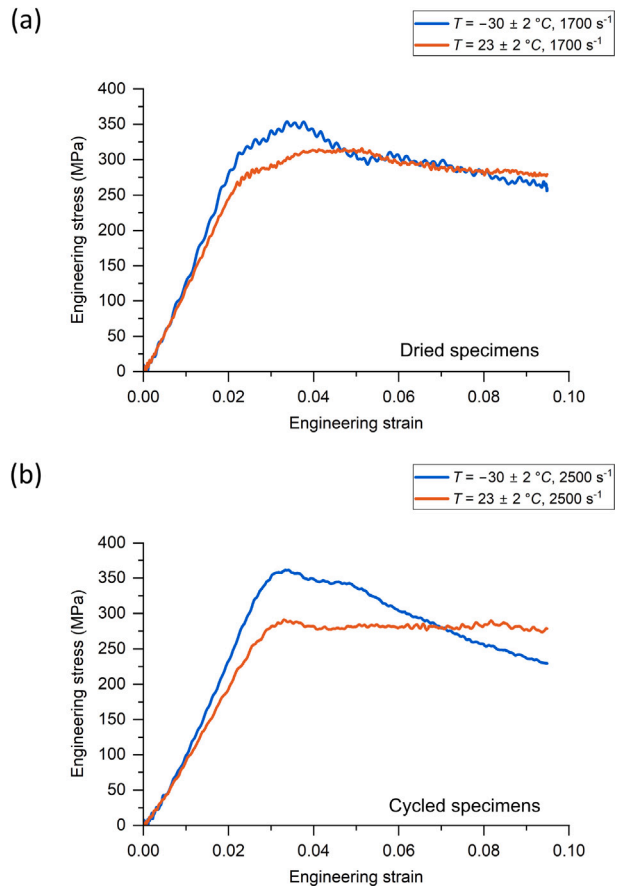

Fig. 6. Stress–strain curve of (a) dried and (b) cycled specimens at room and low temperatures.

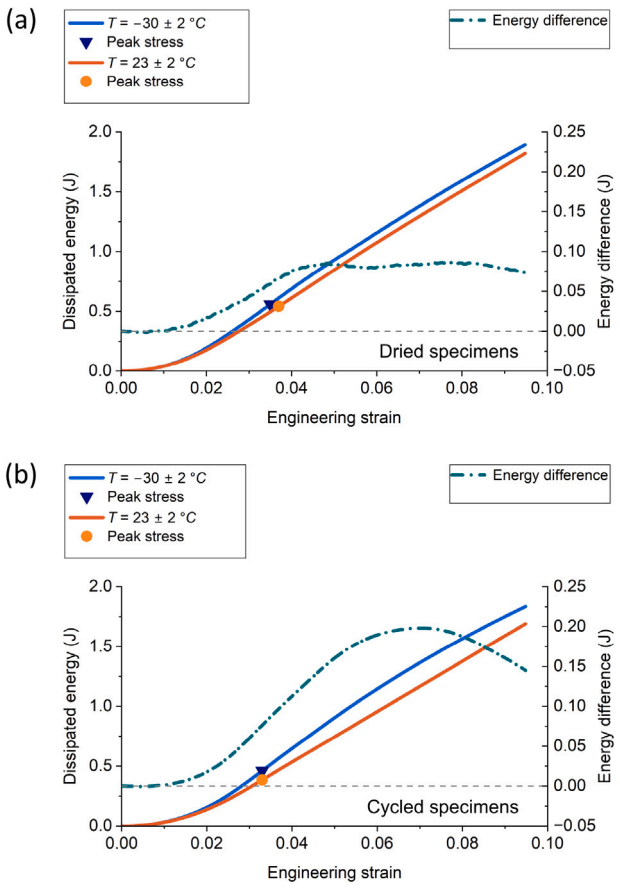

Fig. 7. Energy dissipated through the specimens as the function of strain: (a) dried and (b) cycled specimens.

using a directional image analysis method [35] facilitated by the ImageJ OrientationJ plugin. Explicit explanation of these two analyses is presented in the following section.

3. Results and discussion

3.1. Specimen microstructures

Fig. 3 presents the internal microstructure of the tested CFRP laminates examined by using synchrotron-based X-ray μCT prior to the HSR loading. It shows the tested laminates consist of 16 layers of CFRP plies (Fig. 3a) with densely packed (around 80%) 5 μm-diameter carbon fibres (Figs. 3b) in the orientations of ±45° and symmetrically arranged about the central axis. By making a cutting plane across two adjacent plies on either side of the symmetry axis (Figs. 3b) and applying directional image analysis (Fig. 3c) [35], it can be seen that the +45° and −45° fibre plies were laid up in turn. Each ply is approximately 170 μm in thickness and glued by a thin layer (about 15 μm) of the matrix material, which leads to a total thickness of ~3000 μm. Spherical voids with diameter in the range 5 to 20 μm are spread evenly within the inter-ply glue layers without coalescence to each other (Fig. 3d). No obvious defects can be identified in the dried and cycled CFRP specimens. It should be noted that the voids are too small to be resolved by the indirect MHz XPCI in the dynamic experiments (1× magnification).

3.2. Mechanical properties

QS uni-axial compression tests on both dried and cycled specimens were performed and analysed (Fig. 4) to establish a baseline for HSR mechanical property analysis in the present research. An example of force recorded from the input and output bar during HSR loading tests is present in Fig. 5 which demonstrates equilibrium was reached during the dynamic loading.

The obtained specimen stress σ versus strain ε curves in Fig. 6 show that there is a significant strength increase at room temperature for both dried and cycled specimens under HSR loading compared to the ones tested at QS loading. For the HSR loading tests, the specimens tested at low temperatures have noticeably higher strength (about 10% for dried and 20% for cycled specimens) and apparent stiffness than their room temperature counterparts, although they all reached their maximum stress at approximately $\varepsilon = 3.5\%$. Similar findings were also reported by Liu et al. [9] and Wang et al. [36]. After the peak, the flow stress in the low-temperature specimens dropped rapidly with increasing strain, whereas the room-temperature specimens maintained a stable flow stress. This observation is more prominent for the cycled specimens, as shown in Fig. 6b. Regarding the cycling effect on the specimen strength, the dried specimen at room temperature has a higher strength than the cycled specimen, although the test strain rate was lower for the dry specimen compared to the cycled. This agrees with the experimental results on the tensile tests of a unidirectional-90 CFRP laminate reported by Meng et al. [15]. A similar trend can also be observed from the QS test results shown in Fig. 4. However, the cycling effect on the specimens tested at low temperatures (both dried and cycled) is not very obvious in terms of strength.

This observed difference in behaviour should mainly be driven by the thermophysical behaviour of the epoxy matrix, since the mechanical properties of carbon fibres are comparatively insensitive at temperatures below 400 °C [14,37]. The matrix on the other hand

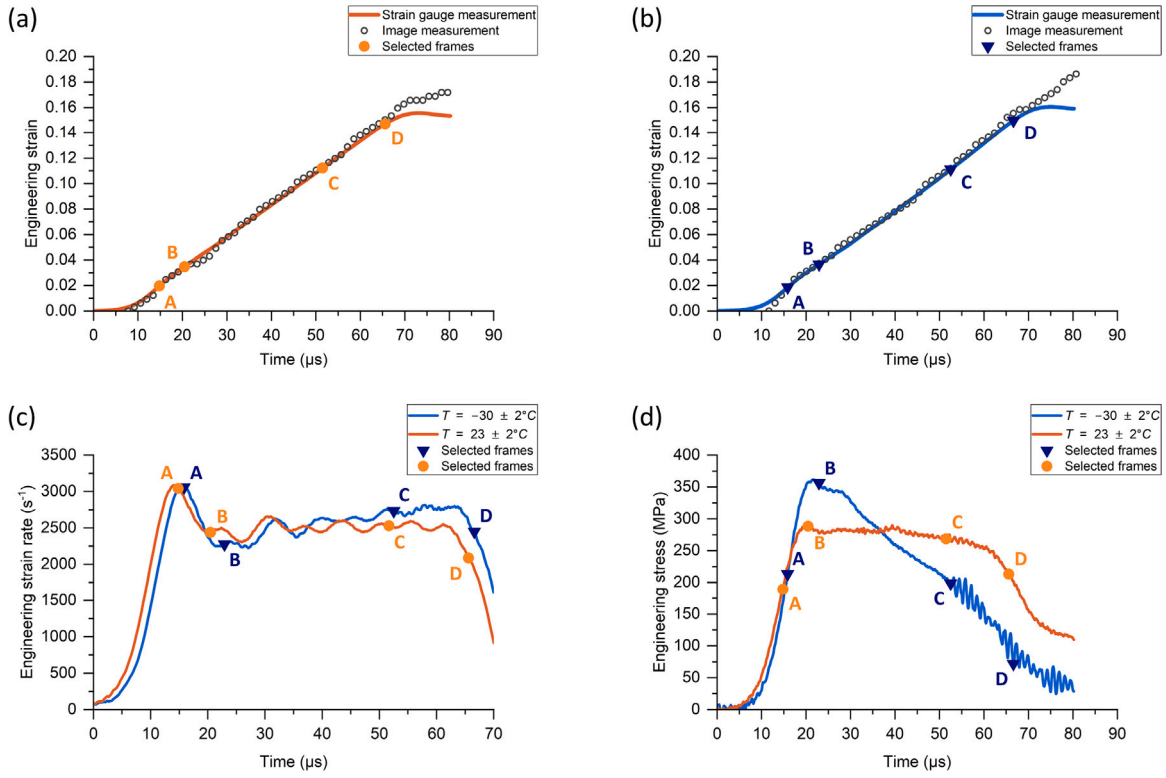

Fig. 8. Mechanical response of the cycled specimens as a function of time t: (a) engineering strain at room temperature, (b) engineering strain at low temperature; (c) engineering strain rate, and (d) engineering stress. t is referenced to the first loading of the specimen.

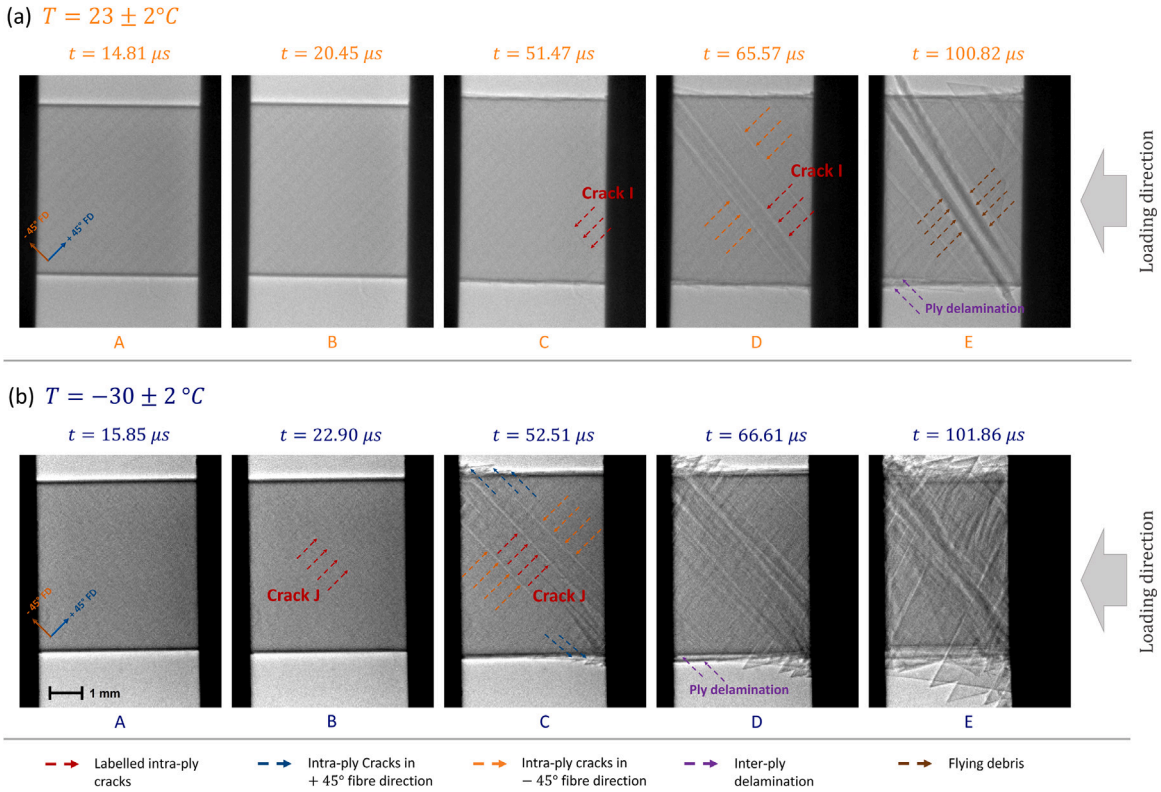

Fig. 9. Subsurface failure initiation and evolution for the (a) room- and (b) low-temperature specimens under HSR loading presented by five key frames captured using synchrotron-based MHz XPCI. The selected frames from the room- and low-temperature specimens are approximately equivalent in time and strain. Damage in the low-temperature specimen initiated earlier and developed faster than that in the room-temperature specimen. The earliest damage that can be observed for the room-temperature specimen is in Frame C (t = 51.47 μs, $\varepsilon \simeq 11.2\%$), whereas that for the low-temperature specimen is in Frame B (t = 22.90 μs, $\varepsilon \simeq 3.7\%$).

Table 2
Summary of mechanical response and damage state for the (a) room- and (b) low-temperature specimens with impact progression. Fibre direction (FD) shown was estimated based on the overall deformation of the specimens measured from the images in both parallel and perpendicular directions to the loading.

(a) $T = 23 \pm 2$ °C					
Frame label	A	B	C	D	E
Time after impact t, μs	14.81	20.45	51.47	65.57	100.82
Gauge strain ε, % (Fig. 8)	2.0	3.5	11.2	14.7	–
Image strain ε_I, % (Fig. 8)	1.8	3.4	11.4	15.0	16.0
Gauge stress σ, MPa (Fig. 8)	189.03	288.30	268.35	212.98	–
Stress state (Fig. 8)	Raising elastically	Peak stress	6% strength lost	27% strength lost	–
Damage state (Figs. 9, 10 and 11)	No crack	No crack	Intra-ply crack emerged	Minor inter-ply delamination	Inter-ply delamination
Fibre direction (FD) (based on ε_I)	±45.5°	±46.0°	±48.1°	±49.0°	±49.2°
Crack direction (Figs. 10 and 11)	–	–	−47.0°	$-50.0 \pm 2°$	$\pm 51 \pm 2°$
(b) $T = -30 \pm 2$ °C					
Frame label	A	B	C	D	E
Time after impact t, μs	15.85	22.90	52.51	66.61	101.86
Gauge strain ε, % (Fig. 8)	1.9	3.7	11.1	15.0	–
Image strain ε_I, % (Fig. 8)	1.9	3.7	11.2	15.5	24.8
Gauge stress σ, MPa (Fig. 8)	213.28	356.31	198.55	71.82	–
Stress state (Fig. 8)	Raising elastically	Peak stress	50% strength lost	80% strength lost	–
Damage state (Figs. 9, 10 and 11)	No crack	Intra-ply crack emerged	Intra-ply cracks in both directions	Inter-ply delamination	Structure collapsed
Fibre direction (FD) (based on ε_I)	±45.5°	±46.0°	±48.4°	±49.8°	±53.0°
Crack direction (Figs. 10 and 11)	–	−45.5°	$\pm 47.0 \pm 2°$	$\pm 50.0 \pm 2°$	$\pm 56.0 \pm 5°$

becomes stiffer at low temperatures owing to the reduced internal energy and mobility of molecule chain segments [38]. Consequently, the interaction between fibre and matrix might be less important compared to that at room temperature, as the increased matrix strength forms most of the load resistance in low-temperature specimens before the peak stress. Additionally, the absolute coefficient of thermal expansion (CTE) of epoxy resin and ice introduced by hygrothermal cycling can be significantly higher than that of carbon fibres [39], which will alter the state and distribution of residual stress within the material at low temperature, and may influence the mechanical response.

3.3. Energy dissipation

The energy dissipated through specimen deformation and damage, W, is shown with respect to engineering strain, ε, for each tested condition in Fig. 7. In the case of the dried specimens, it can be seen that W exhibits a quicker rise when tested at low temperatures before levelling off after the peak stress is achieved. This is a consequence of the higher apparent stiffness and peak stress for the cooled specimen, as shown in Fig. 6a. A similar behaviour is observed for the cycled specimens, where a greater degree of strain energy is initially dissipated at the lower temperature. A notable key difference here however is the reversal in energy dissipation which arises due to the much steeper drop in load-carrying capacity for the low-temperature specimen. The testing temperature seems to have a more prominent effect in cycled specimens indicated by the higher energy difference shown in Fig. 7b possibly resulting from the presence of moisture. In terms of overall energy dissipation, no significant difference can be found up to $\varepsilon \simeq 9.5\%$ between dried and cycled specimens. Although the low specimens still demonstrate higher energy dissipation for both ageing cases relative to their room-temperature counterparts, the stress declines more rapidly after the peak in the cycled specimens, suggesting room-temperature specimens might overtake at larger strain.

Previous studies on the behaviour of CFRP during impact loading indicate that this drop in toughness can be attributed to the reduced ductility of the matrix at low temperature, resulting in a decreased threshold for damage [12,40]. This effect is particularly evident in the ±45° CFRP laminates tested in the present study, implying that the mechanical response and failure are dominated by the matrix material [41]. However, the conventional strain gauge measurement cannot provide further information or direct indication to elaborate damage mechanisms associated with this behavioural difference at different temperatures under HSR. Therefore, synchrotron-based MHz XPCI was introduced in this study to perform *in-situ* observation of this impact and subsurface failure event.

3.4. Observed damage initiation

Real-time X-ray phase contrast imaging, synchronised to the HSR loading, was used to investigate the nature and evolution of damage with respect to the bulk mechanical conditions measured using the strain gauges. X-ray images of the cycled specimens were selected and analysed in this section since they demonstrated the clearest difference in response between low and room temperature possibly by virtue of the moisture present. Fig. 8a and 8b show the comparison between axial strain history as measured by the strain gauges and XPCI for the room- and low-temperature specimens, respectively. It can be seen that there is good agreement between the two measurement techniques from ∼ 15–70 μs, during which time the strain-rate was stable (see Fig. 8c). Thus, all time-based damage analyses were selected within these regions.

Fig. 9 demonstrates the subsurface damage progression in both room- and low-temperature specimens with respect to time t by presenting five key XPCI frames — Frames A to E. Table 2 summarises the main damage observation with the associated stress and strain states. Although the similar strain development between two specimens before $t = 70$ μs, the cracks in the low-temperature specimen can be clearly identified earlier than that in the room-temperature specimen. At the very early impact stage (Frame A for both specimens in Fig. 9), no internal structural change can be observed from the images regardless of temperature. The first evidence of cracks in the low-temperature specimen can be found at approximately $t = 22.90$ μs (Crack J in Frame B, Fig. 9b), at which time the specimen was near its peak stress (Fig. 8d) at $\varepsilon \simeq 3.7\%$. In comparison, no similar features can be recognised at a similar time and strain in the room-temperature specimen (Frame B, Fig. 9a), where cracks are not visible until $t = 51.47$ μs and $\varepsilon \simeq 11.2\%$ (Crack I in Frame C, Fig. 9a). At Frame C (first observed crack) in Fig. 9a, the stress in the room-temperature specimen had experienced a slight drop (about 6%) relative to Frame B (peak stress), but it was still maintained at roughly the same level.

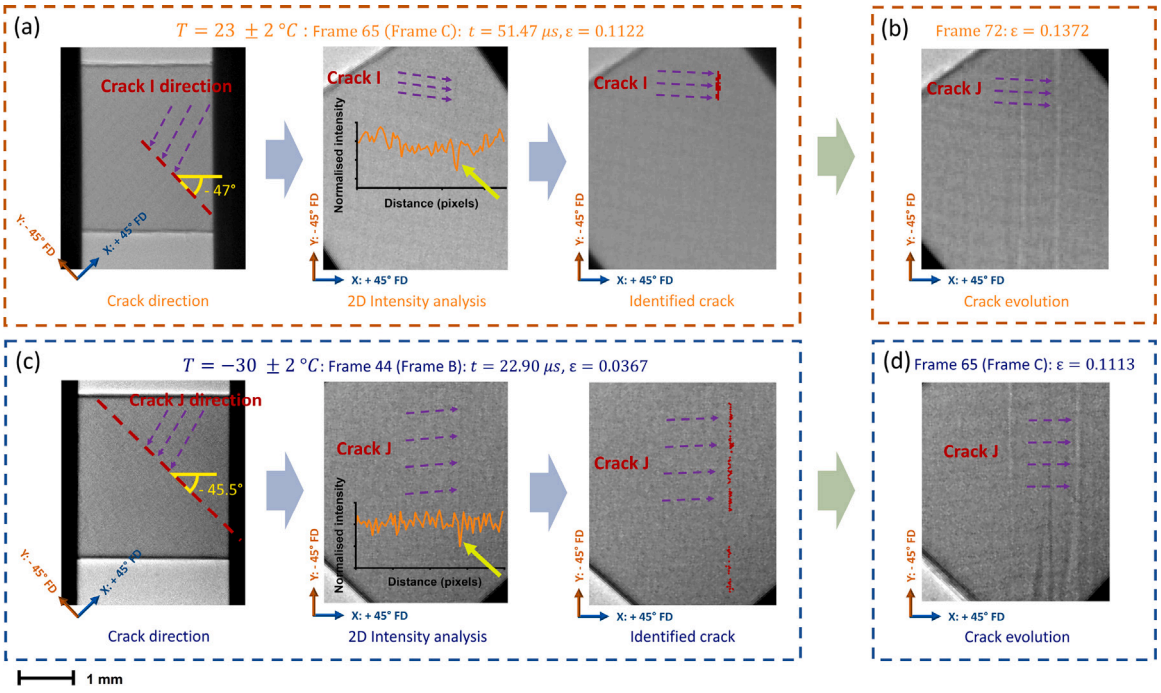

Fig. 10. Identifying the initiated cracks and their later stage development in obtained X-ray radiography. (a) Initiated crack identification and (b) its development for the room-temperature specimen, and (c) initiated crack identification and (d) its development for the low-temperature specimen. By calculating the average intensity along the crack directions, and plotting it along the perpendicular distance, the initiated narrow cracks can be visualised by sudden intensity changes, as shown in (a) and (c).

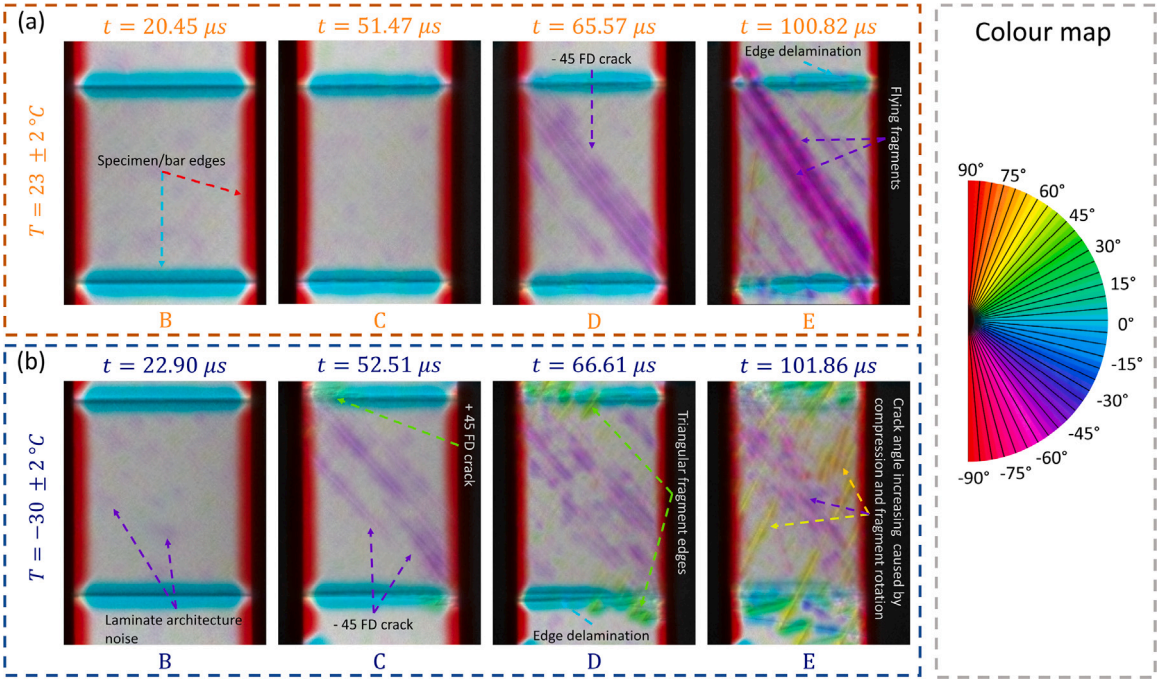

Fig. 11. Cracks highlighted on the obtained X-ray radiography based on directional features: (a) room- and (b) low-temperature specimens. For the room-temperature specimen, cracks in −45° can be recognised in Frame D and E, but no clear cracks are highlighted in +45°. Minor inter-ply delamination is shown at the upper edge in Frame D and at the both upper and lower edges in Frame E. In comparison, both ±45° FD cracks can be seen starting from Frame C in the low-temperature specimen. Obvious inter-ply delamination can be identified in Frame D and E. (For interpretation of the references to colour in this figure legend, the reader is referred to the web version of this article.).

At the early impact stage, all identified crack openings were deemed to be subpixel in size, and the crack interfaces were assumed to be largely in contact. Thus, no measurable change in X-ray transmission would be produced, and any intensity change at the detector would be dominated by phase effects. To better accommodate the directional feature of observed damage revealed by XPCI in the present study, a 2D crack identification method was applied, where the average intensity normal to the supposed crack propagation direction was determined to reduce sensitivity to Poisson noise in the image. Fig. 10a presents the 2D intensity analysis for the room-temperature specimen, where a prominent drop in intensity (highlighted by a yellow–green arrow) can be observed in Frame C ($\epsilon \simeq 11.2\%$) with an approximate length of

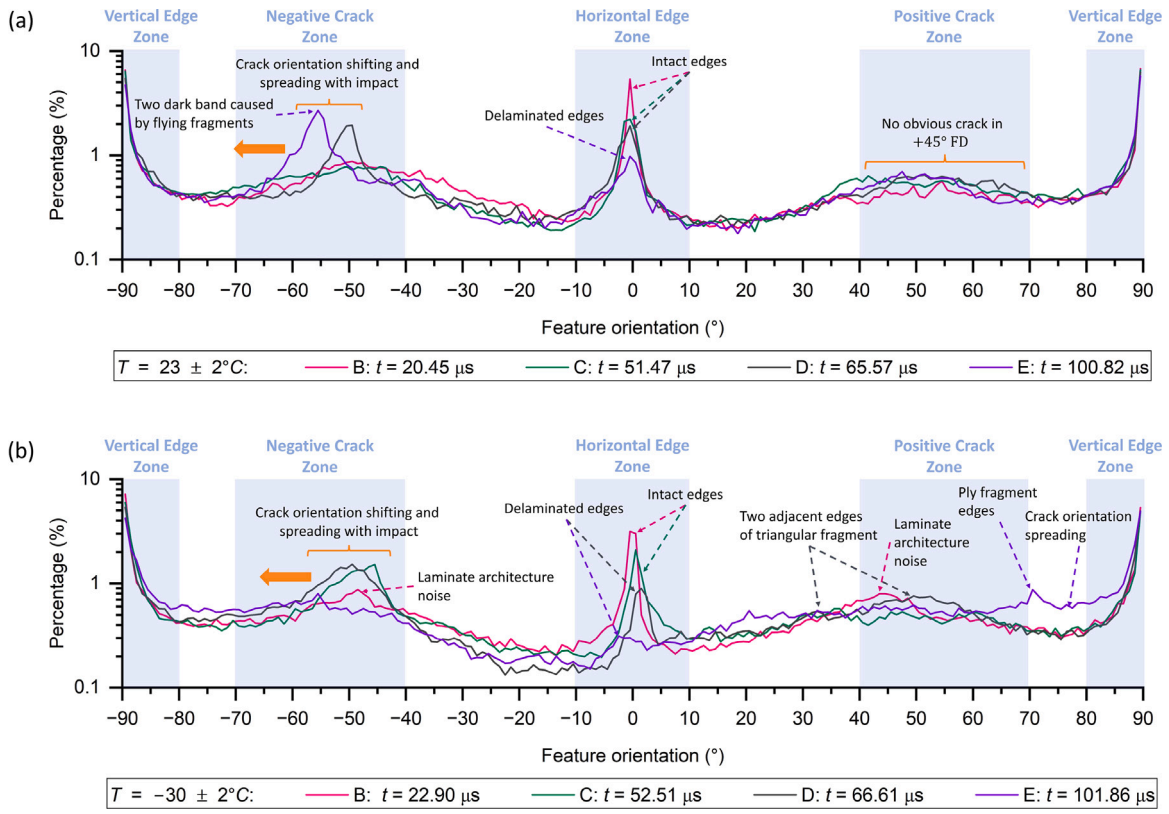

Fig. 12. Orientation distribution for the XPCI radiography: (a) room- and (b) low-temperature specimen. Vertical Edge Zone: specimen/bar vertical edge dominated zone, Negative Crack Zone: negative crack (−45° FD) dominated zone, Horizontal Edge Zone: specimen horizontal edge dominated zone, Positive Crack Zone: positive crack (+45° FD) dominated zone. The peaks in Vertical Edge Zones are mainly caused by the left and right edges of bars and specimens; the peaks in Horizontal Edge Zones result from the upper and lower edges of the specimens; the peaks in Negative Crack Zones and Positive Crack Zones are the representations of generated cracks that orientates in similar directions. (For interpretation of the references to colour in this figure legend, the reader is referred to the web version of this article.).

0.5 mm and angle of −47.0°. It results from local interference (phase contrast) in the propagated X-rays when passing through the newly generated Crack I. With further axial strain, the crack is seen to grow in width resulting in decreased X-ray absorption as shown in Fig. 10b.

A similar analysis was conducted for the low-temperature specimen (Fig. 10c) revealing an early-stage crack (Crack J) at Frame B ($\varepsilon \simeq 3.7\%$). Two narrow crack traces with an approximate length of 2 mm and 0.8 mm align on the same −45.5° line, which coincides with the −45° fibre direction (FD) at this strain (see Table 2). This placement suggests the crack had propagated along the fibres. However, at a similar strain level when the first crack is initiated in the room-temperature specimen (*i.e.*, $\varepsilon \simeq 11.2\%$), more cracks have emerged in the central region of the low-temperature specimen, with some having grown significantly (Frame C, Fig. 10d).

3.5. Observed damage evolution

Frame D to E in Fig. 9a and C to E in Fig. 9b present the rapid damage evolution in the room- and low-temperature specimens, respectively. At a similar strain level (refer to Table 2), the low-temperature specimen demonstrates a noticeably higher degree of damage. Fig. 11 illustrates XPCI highlighted using the directional feature analysis method, with the resulting orientation distributions plotted in Fig. 12. While cracks can be seen in both +45° (top-left and bottom-right corner) and −45° (central region) FD at Frame C in Fig. 11b, no damage can yet be identified at Frame C in Fig. 11a. This is also reflected by the clear peak observed in the Negative Crack Zone of Curve C in Fig. 12b, whereas the Curve C in the Negative Crack Zone in Fig. 12a remains relatively flat and even. 50% of the specimen strength had been lost at this strain in the low-temperature specimen compared to only slight strength loss (about 6%) in the room-temperature specimen.

For the room-temperature specimen at $\varepsilon \simeq 14.7\%$, multiple open cracks can be found at an angle of roughly $-50.0 \pm 2°$ to the horizontal axis (see Frame D in Fig. 9a and Fig. 11a) and are well-aligned with the deformed −45° FD indicated by the peak of Curve D at about −50° within the Negative Crack Zone in Fig. 12a. No clear cracks in +45° FD can be identified, which implies that the cracks in +45° fibre plies were still very narrow at this stage. Minor inter-ply delamination can be identified at the top-right and bottom-left corners. At the time of this frame, the stress in the specimen had reduced by about 27% compared to the peak stress.

However, at the nominally equivalent time (Frame D in Fig. 9b and 11b) for the low-temperature specimen, more cracks in both FDs appeared with triangular debris detached and flying away from the specimen in the top-left and bottom-right corners. The orientation of cracks is seen to shift to higher angles to the loading axis in the Negative Crack Zone (Curve D, Fig. 12b). Multiple interfaces are clearly visible at the lower edge of the specimen by virtue of ply delamination, resulting in the broadening of the peak of Curve D compared to Curve C within the Horizontal Edge Zone in Fig. 12b. The specimen has lost more than 85% of its strength at this time. Approximately 35 μs later (Frame E, 9b and 11b), the low-temperature specimen experienced widespread failure. A large number of cracks and detached debris can be observed throughout the radiograph, indicating severe ply breakage in the specimen.

Even at the final loading stage (Frame E, Fig. 9a and 11a), high specimen integrity was still maintained for the room-temperature specimen in contrast to the low-temperature specimen (Frame E, 9b and 11b), similar to the observations by Guedes et al. [5], Sanchez-Saez et al. [8] and Jia et al. [14]. The observable cracks were still in −45° FD plies, although some dark traces (possibly narrow cracks), which are vaguely highlighted in greenish-yellow in Frame E, Fig. 11a,

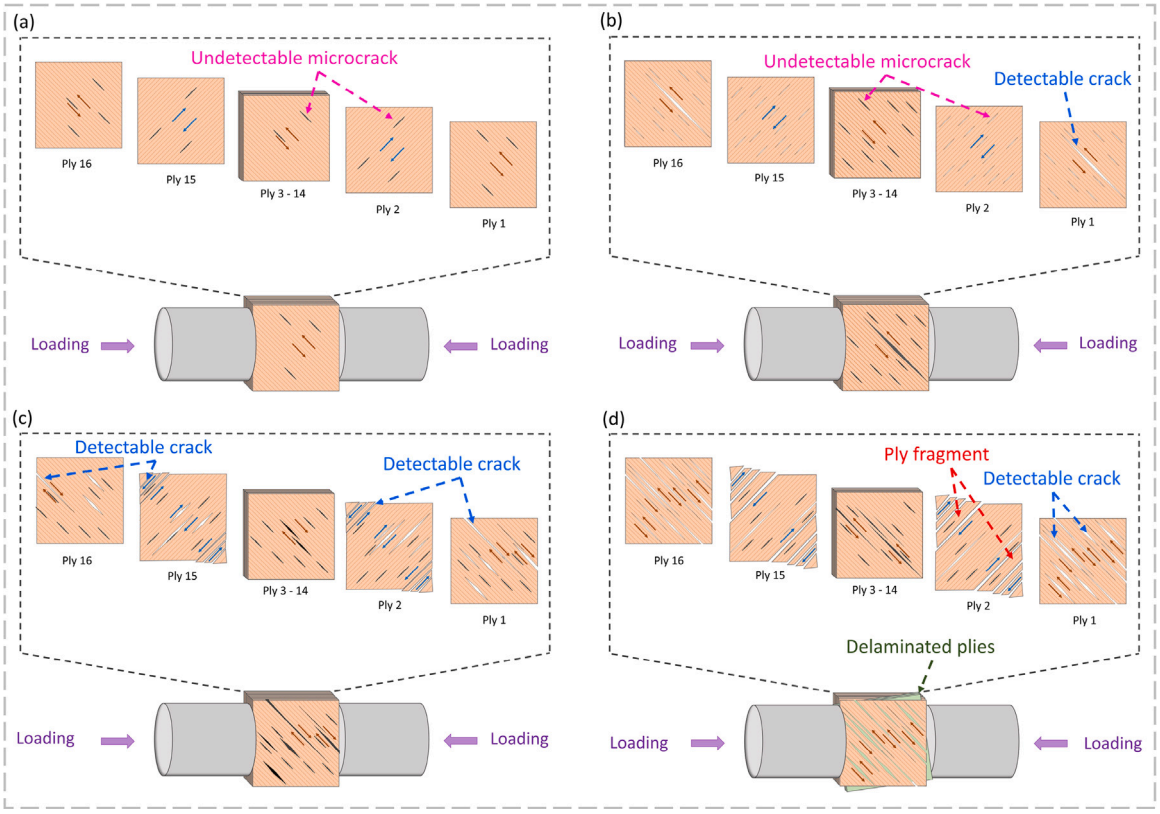

Fig. 13. Schematic of the damage evolution mechanisms of tested CFRP laminates with ply breakdowns: (a) microscale damage in subpixel size (undetectable under XPCI); (b) micro-cracks coalesce and broaden up, form detectable cracks in surface plies; (c) as compression continues, detectable cracks emerge in subsurface plies and in both FDs; (d) detectable cracks grow and cause breakage of the surface plies and ply delamination.

had just started to emerge. Ply delamination is also observed, but is less pronounced than in the low-temperature specimen. This is also reflected by the peaks within the Horizontal Edge Zone in Fig. 12a, which although broadening slightly, remains distinct throughout the compression event. The degree of damage in the room-temperature specimen is evidently lower than that of the low-temperature specimen at a similar ε possibly by virtue of the increased matrix brittleness [13] and residual stresses [42] at the fibre/matrix interface due to the lower temperature.

3.6. Failure mechanism discussion

While it has been shown that damage initiates earlier and progresses more quickly at low temperatures, all specimens appear to share a similar sequence of failure processes, namely, intra-ply cracking at the early stage, followed by a combination of intra-ply cracking and inter-ply delamination at the later stage. Fig. 13 presents a proposed mesoscale damage initiation and evolution mechanism for tested AP CFRP laminates based on these experimental observations and analysis. At early times, although there are no detectable cracks, the change in slope of the stress–strain curves indicates the material might have already undergone internal microstructural changes, possibly intra-ply microcracks. A closer study of the early-stage microscale damage under HSR loading and varying temperatures will be reported in future work.

As dynamic compression continues, intra-ply cracks grow and coalesce, as shown in Fig. 13b and supported by Frame C in Fig. 9a and Frame B in 9b. While large cracks might have already been created (*e.g.*, Frame B, Fig. 9b) possibly by stress concentration as a result of low matrix strain tolerance at low temperatures, the higher plasticity of the matrix at room temperature could enable a more even load distribution in the specimens. The resulting, more-uniform, compressive stress-state might have a positive effect in preventing, or at least delaying, the initiation and growth of cracks [20]. Thus, for CFRP laminates tested at room temperature, cracks with observable size only form at a considerably larger strain (*e.g.*, about 11.2% at Frame c in Fig. 9a) and progress slower than those tested at low temperatures.

Although the obtained X-ray radiography are projections through the entire specimen, prior knowledge of the specimen lay-up and by tracking the crack growth behaviour and timescale for debris generation, it is possible to suggest that the observable crack in both room- and low-temperature specimens first appeared in the front and back surface plies where no lateral and inter-ply shear restraints are acting, as illustrated in Fig. 13b. This is also consistent with the failure observed by Xiao et al. [21] for off-axis dynamic in-plane compression on BB CFRP. It is worth mentioning that the first damage in the room-temperature specimen (intra-ply cracking) was identified at approximately $\varepsilon = 11.2\%$ (Frame C), which is significantly earlier than the first damage captured using visible imaging by Cui et al. [20].

With increasing specimen strain, intra-ply shear stress leads to the increase of intra-ply shear strain and the formation of more intra-ply cracks in both FD directions (see Fig. 13c and supported by Frame C, Fig. 9b and 11b). As the fibres in adjacent plies are arranged perpendicular to each other (+45° and −45°), the intra-ply shear strains generated within adjacent plies are also perpendicular, giving rise to inter-ply shear stress. When the inter-ply shear stress exceeds the shear strength of the inter-ply glue layers, delamination occurs (see Fig. 13d and evidenced by Frame E for the room-temperature specimen and Frame D for the low-temperature specimen), leading ultimately to complete failure of the specimen (*e.g.*, Frame E, Fig. 9b and 11b), as observed by Cui et al. [20].

4. Conclusions

A series of HSR compression tests, synchronised to synchrotron-based MHz X-ray PCI, have been performed on AP CFRP laminates at

room and low temperature to identify the subsurface failure mechanisms responsible for the loss of strength observed at the bulk scale.

Independent of temperature, inter-ply cracking and intra-ply delamination were found to play important roles in the failure of all tested AP CFRP specimens. The observable damage was initiated in the form of intra-ply shear cracking in the surface plies along FDs as the result of the lack of lateral restraint and inter-ply shear resistance on the specimen surface. With continued deformation, the observable damage propagated into sub-layers, but the cracks still remained in good alignment with ply FDs before the associated ply fragment detached from the specimen bodies. Further deformation of specimens gives rise to the subsurface intra-ply shear in different orientations (+45° and −45° FD) between adjacent plies, causing the increase of inter-ply shear and subsequent ply delamination.

In-situ testing temperature was observed to exert notable effects on specimens' mechanical properties and timescale of failure. At low temperatures, both dried and cycled CFRP laminates exhibited higher compressive strength and apparent stiffness, and a higher amount of energy was dissipated from the bar before the peak strength was reached. The low-temperature specimens underwent a rapid strength loss and catastrophic failure, while their room-temperature counterparts demonstrated a more ductile-like behaviour after the peaks. These temperature-dependent differences in strength and energy dissipation were observed to be more prominent in specimens subjected to HTC treatment.

The present research thusly identifies the subsurface mesoscale damage mechanisms in AP CFRP laminates, and correlates this in a time-resolved manner with their mechanical response at low temperatures under HSR compressive loading. This coordinated description of thermo-mechanical and damage response can be used to develop, validate and improve advanced numerical models of CFRP laminates under complex service conditions.

CRediT authorship contribution statement

Xiyao Sun: Writing – original draft, Visualization, Validation, Methodology, Investigation, Formal analysis, Data curation, Conceptualization. **David Sory:** Writing – review & editing, Methodology, Investigation, Formal analysis. **Kai Liu:** Writing – review & editing, Validation, Conceptualization. **Bratislav Lukić:** Data curation, Methodology, Writing – review & editing. **David Simonian:** Investigation. **Kwan Lok Wong:** Investigation. **Alexander Rack:** Writing – review & editing, Resources. **David Chapman:** Writing – review & editing, Supervision, Methodology. **Nik Petrinic:** Writing – review & editing, Resources, Funding acquisition. **Daniel Eakins:** Writing – review & editing, Supervision, Resources, Project administration, Funding acquisition.

Declaration of competing interest

The authors declare that they have no known competing financial interests or personal relationships that could have appeared to influence the work reported in this paper.

Data availability

Data will be made available on request.

Acknowledgements

The authors would like to acknowledge Rolls-Royce plc, for their continued support of the University Technology Centre for Solid Mechanics at the University of Oxford. In addition, the authors gratefully acknowledge the funding for this research provided by Innovate UK grant 113190:FANTASTICAL (FAN Testing And STatistical Integrity CALibration). The ESRF, Grenoble, France is acknowledged for providing beamtime and assistance under Beamtime Proposal MA-5715. The authors would also like to thank the workshop team within the Impact and Shock Mechanics Laboratory, Begbroke Science Park for the preparation of the specimens and equipment.

References

[1] Clyne TW, Hull D. An introduction to composite materials. Third ed.. Cambridge; 2019.
[2] Irving PE, Soutis C. Polymer composites in the aerospace industry. San Diego: Elsevier Science & Technology; 2019.
[3] Wang K, Young B, Smith ST. Mechanical properties of pultruded carbon fibre-reinforced polymer (CFRP) plates at elevated temperatures. Eng Struct 2011;33(7):2154–61.
[4] Hosur MV, Alexander J, Vaidya UK, Jeelani S. High strain rate compression response of carbon/epoxy laminate composites. Compos Struct 2001;52:405–17.
[5] Guedes RM, de Moura MF, Ferreira FJ. Failure analysis of quasi-isotropic CFRP laminates under high strain rate compression loading. Compos Struct 2008;84(4):362–8.
[6] Zhao C, Zhou Z, Zhao C, Zhu H, Zhang K, Zhong J, et al. Research on compression properties of unidirectional carbon fiber reinforced epoxy resin composite (UCFREP). J Compos Mater 2021;55(11):1447–58.
[7] Ochola RO, Marcus K, Nurick GN, Franz T. Mechanical behaviour of glass and carbon fibre reinforced composites at varying strain rates. Compos Struct 2004;63(3–4):455–67.
[8] Sánchez-Sáez S, Gómez-Del Río T, Barbero E, Zaera R, Navarro C. Static behavior of CFRPs at low temperatures. Composites B 2002;33:383–90.
[9] Liu J, Zhou Z, Ma L, Xiong J, Wu L. Temperature effects on the strength and crushing behavior of carbon fiber composite truss sandwich cores. Composites B 2011;42(7):1860–6.
[10] Wei W, Rongjin H, Chuanjun H, Zhao Y, Li S, Laifeng L. Cryogenic performances of T700 and T800 carbon fibre-epoxy laminates. In: IOP conference series: materials science and engineering. Vol. 102, (1). Institute of Physics Publishing; 2015.
[11] Shi H, Sun B, Liu Q, Yang Z, Zhang Y. Properties of cryogenic epoxy resin matrix composites prepared by RTM process. In: 20th international conference on composite materials. 2015.
[12] Gómez-del Río T, Barbero E, Zaera R, Navarro C. Dynamic tensile behaviour at low temperature of CFRP using a split Hopkinson pressure bar. Compos Sci Technol 2005;65(1):61–71.
[13] Ou Y, Zhu D, Zhang H, Yao Y, Mobasher B, Huang L. Mechanical properties and failure characteristics of CFRP under intermediate strain rates and varying temperatures. Composites B 2016;95:123–36.
[14] Jia Z, Li T, Chiang Fp, Wang L. An experimental investigation of the temperature effect on the mechanics of carbon fiber reinforced polymer composites. Compos Sci Technol 2018;154:53–63.
[15] Meng J, Wang Y, Yang H, Wang P, Lei Q, Shi H, et al. Mechanical properties and internal microdefects evolution of carbon fiber reinforced polymer composites: Cryogenic temperature and thermocycling effects. Compos Sci Technol 2020;191.
[16] Weaver CW, Williams JG. Deformation of a carbon-epoxy composite under hydrostatic pressure. J Mater Sci 1975;10(8):1323–33.
[17] Pinheiro D, Longo O, Nascimento G, Couri G. Use of composite materials in carbon fiber for the recovery of small slab – calculation by analytical and computational methods. Int J Compos Mater 2017;7(1):1–7.
[18] Wang L, Kawaguchi K, Xu J, Han Q. Effects of transverse constraints on the longitudinal compressive strength of unidirectional CFRP pultruded plates and rods. Compos Struct 2019;207:740–51.
[19] Zhang X, Shi Y, Li ZX. Experimental study on the tensile behavior of unidirectional and plain weave CFRP laminates under different strain rates. Composites B 2019;164(June 2018):524–36.
[20] Cui H, Thomson D, Pellegrino A, Wiegand J, Petrinic N. Effect of strain rate and fibre rotation on the in-plane shear response of ±45° laminates in tension and compression tests. Compos Sci Technol 2016;135:106–15.
[21] Xiao J, Wu Z, Pan Z, Ouyang W, Shi L. Analysis of in-plane compression failure mechanism in carbon fiber braided composite with different off-axial angles. J Compos Mater 2022;56(13):2029–46.
[22] Garcea SC, Wang Y, Withers PJ. X-ray computed tomography of polymer composites. Compos Sci Technol 2018;156:305–19.
[23] Zwanenburg EA, Norman DG, Qian C, Kendall KN, Williams MA, Warnett JM. Effective X-ray micro computed tomography imaging of carbon fibre composites. Composites B 2023;258.
[24] Ni X, Kopp R, Kalfon-Cohen E, Furtado C, Lee J, Arteiro A, et al. In situ synchrotron computed tomography study of nanoscale interlaminar reinforcement and thin-ply effects on damage progression in composite laminates. Composites B 2021;217.
[25] Wang Y, Emerson MJ, Conradsen K, Dahl AB, Dahl VA, Maire E, et al. Evolution of fibre deflection leading to kink-band formation in unidirectional glass fibre/epoxy composite under axial compression. Compos Sci Technol 2021;213(March):108929.
[26] Wingate BP, Czabaj MW. In-situ imaging of flexure-induced fracture in tape-laminate composites using high-resolution X-ray computed tomography. Compos Sci Technol 2022;220.
[27] Watanabe T, Takeichi Y, Niwa Y, Hojo M, Kimura M. Nanoscale in situ observations of crack initiation and propagation in carbon fiber/epoxy composites using synchrotron radiation X-ray computed tomography. Compos Sci Technol 2020;197.

[28] Nie Y, Parab ND, Chu J-m, Kim G, Sun T, Fezzaa K, et al. Dynamic crack propagation from a circular defect in a unidirectional carbon fiber reinforced plastic composite. J Compos Mater 2018;52(25):3539–47.
[29] Pournoori N, Corrêa Soares G, Lukić B, Isakov M, Belone MCL, Hokka M, et al. In situ damage characterization of CFRP under compression using high-speed optical, infrared and synchrotron X-ray phase-contrast imaging. Composites A 2023;175.
[30] ASTM. Standard test method for moisture absorption properties and equilibrium conditioning of polymer matrix composite materials. Technical Report, American Society for Testing and Materials; 2004.
[31] Gray GT. Classic Split-Hopkinson Pressure Bar Testing. In: Kuhn H, Medlin D, editors. Mechanical Testing and Evaluation. 8, ASM International; 2000, p. 462–76.
[32] Weitkamp T, Tafforeau P, Boller E, Cloetens P, Valade JP, Bernard P, et al. Parallel-beam imaging at the ESRF beamline ID19: Current status and plans for the future. In: AIP conference proceedings. Vol. 1234, American Institute of Physics Inc.; 2010, p. 83–6.
[33] Escauriza EM, Olbinado MP, Rutherford ME, Chapman DJ, Jonsson JCZ, Rack A, et al. Ultra-high-speed indirect x-ray imaging system with versatile spatiotemporal sampling capabilities. Appl Opt 2018;57(18):5004.
[34] Buakor K, Zhang Y, Birnšteinová Š, Bellucci V, Sato T, Kirkwood H, et al. Shot-to-shot flat-field correction at X-ray free-electron lasers. Opt Express 2022;30(7):10633.
[35] Püspöki Z, Storath M, Sage D, Unser M. Transforms and operators for directional bioimage analysis: A survey. In: Focus on bio-image informatics. Vol. 219, Springer Verlag; 2016, p. 69–93.
[36] Wang H, Sun B, Gu B. Coupling effect of temperature and braided angle on compressive behaviors of 3D braided carbon–epoxy composite at low temperature. J Compos Mater 2017;51(18):2531–47.
[37] Feih S, Mouritz AP. Tensile properties of carbon fibres and carbon fibre-polymer composites in fire. Composites A 2012;43(5):765–72.
[38] Robert D, Caserio C. Basic principles of organic chemistry. second ed.. CA: W.A. Benjamin; 1977.
[39] Chung DDL. Carbon composites : composites with carbon fibers, nanofibers, and nanotubes. second ed.. Kidlington, Oxford, United Kingdom; 2016.
[40] Chen ZK, Yang JP, Ni QQ, Fu SY, Huang YG. Reinforcement of epoxy resins with multi-walled carbon nanotubes for enhancing cryogenic mechanical properties. Polymer 2009;50(19):4753–9.
[41] Thomson D, Quino G, Cui H, Pellegrino A, Erice B, Petrinic N. Strain-rate and off-axis loading effects on the fibre compression strength of CFRP laminates: Experiments and constitutive modelling. Compos Sci Technol 2020;195.
[42] Reed RP, Golda M. Cryogenic properties of unidirectional composites. Cryogenics 1994;34(11):909–28.